Article

Not peer-reviewed version

The Seeds Combining Pyrrolidine Controlling the Framework Al Distribution of FER Zeolites to Enhance Its Performance in the Skeletal Isomerization of n-Butene

Jinlong Fan , Xuedong Zhu * , Fan Yang , Yarong Xu , Lantian Chen

Posted Date: 3 September 2024

doi: 10.20944/preprints202409.0175.v1

Keywords: FER zeolites; seed; Pyrrolidine; Al distribution; *n*-Butene; Skeletal isomerization

Preprints.org is a free multidiscipline platform providing preprint service that is dedicated to making early versions of research outputs permanently available and citable. Preprints posted at Preprints.org appear in Web of Science, Crossref, Google Scholar, Scilit, Europe PMC.

Copyright: This is an open access article distributed under the Creative Commons Attribution License which permits unrestricted use, distribution, and reproduction in any medium, provided the original work is properly cited.

Preprints.org (www.preprints.org) | NOT PEER-REVIEWED | Posted: 3 September 2024

doi:10.20944/preprints202409.0175.v1

Disclaimer/Publisher's Note: The statements, opinions, and data contained in all publications are solely those of the individual author(s) and contributor(s) and not of MDPI and/or the editor(s). MDPI and/or the editor(s) disclaim responsibility for any injury to people or property resulting from any ideas, methods, instructions, or products referred to in the content.

Article

The Seeds Combining Pyrrolidine Controlling the Framework Al Distribution of FER Zeolites to Enhance Its Performance in the Skeletal Isomerization of n-Butene

Jinlong Fan [1,2], Xuedong Zhu [1*], Fan Yang [1], Yarong Xu [2] and Lantian Chen [2]

[1] State Key Laboratory of Chemical Engineering, East China University of Science and Technology, Shanghai 200237, china; fanjlws@petrochina.com.cn (F.J.); yfan@ecust.edu.cn (Y.F.)
[2] Research Institute of Urumqi Petrochemical Company, Petrochina Company Limited, Urumqi 830019, china; xuyrws@petrochina.com.cn (X.Y.); chenltws@petrochina.com.cn (C.L.)
* Correspondence: xdzhu@ecust.edu.cn; Tel.: +86-21-64251005

Abstract: **FER** zeolites has a unique framework structure and acid distribution, and is widely studied as a catalyst for reactions such as n-butene skeletal isomerization and dimethyl ether carbonylation. The BAS located in the 10-MR of **FER** zeolites serves as the active site for the isomerization reaction of n-butene skeletal to produce isobutene. In contrast, the acid site found in the 8-MR is prone to side reactions, such as polymerization and cracking, which can adversely affect the selectivity of isobutene. This study prepared five types of **FER** zeolites using different method, inducing Na-form or H-form crystal seeds without organic structure directing agents (OSDAS), using pyridine alone as a template, and combining the seeds with pyridine. The differences in the structure and acid distribution of the five zeolites were investigated, as well as their catalytic performance for the the skeletal isomerization of n-Butene. Experiments and characterization results showed that under hydrothermal synthesis conditions, the FER-PY+SH zeolites synthesized by using both H-form zeolites seeds and pyridine exhibited the highest aluminum concentrations at T1 and T3 positions, along with the greatest BAS of 10-MR. This unique composition contributed to the highest selectivity of isobutene. The FER-PY+SH catalyst was continuously used for 720 hours at 350 °C, 0.1 MPa, and n-butene mass space velocity of 2.0 h^{-1} for three recycles on 2160 h. During this period, the conversion of n-butene over 39%, while the selectivity of isobutene exceeded 95%.The catalyst exhibited excellent stability and activity.

Keywords: **FER** zeolites; seed; Pyrrolidine; Al distribution; *n*-Butene; Skeletal isomerization

1. Introduction

Isobutene is an important basic organic chemical raw material, which can be used to produce many high value-added products, including butyl rubber, polyisobutylene, methyl tert butyl ether (MTBE), methyl methacrylate, etc. One of the primary industrial production methods its production involves the skeletal isomerization of n-butene to generate isobutene [1–3]. In the past few decades, extensive research has focused on the production of isobutene through theskeleton isomerization of butene, utilizing various catalysts such as phosphoric acid, metal halides, aluminum oxide, phosphated and halogenated aluminum oxide, and zeolite molecular sieves [4,5]. The pore structure of **FER** zeolite includes two vertically intersecting two-dimensional pore systems: an 8-membered ring pore (0.35 × 0.48 nm) along the [010] direction, a 10 membered ring (10-MR) pore (0.43 × 0.55 nm) along the [001] direction, and a magnesium alkali zeolite cage with a diameter of approximately 0.6-0.7 nm formed by the intersection of 6 membered ring and 8-MR [6,7]. **FER** zeolite is currently highest-performance n-butene skeleton isomerization catalyst and was successfully applied in industrial applications in the 1990s [8].

© 2024 by the author(s). Distributed under a Creative Commons CC BY license.

Numerous studies have demonstrated that the B acid site (BAS) located on the 10-MR in **FER** zeolite as a selective active site for catalyzing the skeleton isomerization of n-butene to produce isobutene. In contrast, the L acid site (LAS) and BAS located on the 8-MR can exacerbate the occurrence of side reactions such as butene polymerization and cracking [9–13]. As is well known, molecular sieves are crystal compounds composed of TO4 (T atoms are generally Si or Al) tetrahedra according to certain rules. Their acidity mainly arises from the introduction of protons, which balance the negative charge of aluminum atoms in the molecular sieve framework. It can be seen that the catalytic performance of zeolites is closely linked to the strength and position of acid sites. The strength and position of these acid sites are directly influenced by the distribution of Al atoms within the zeolite framework [14–17]. According to relevant information from the International Zeolite Association (IZA), the framework T atom of **FER** molecular sieve exhibit four distinct positions, namely the T1/T2/T3 position,which can be connected to a 10 membered ring or **FER** cage, and the T4 position, which is solely connected connected through a **FER** cage (note: labels of T atoms have been unified according to the **FER** framework in the IZA). Xiong et al. [18–20] studied the skeletal aluminum atoms at four different T-positions of **FER** molecular sieves. The experimental characterization and theoretical calculation results were consistent. The ^{27} Al NMR isotropic chemical shifts of the aluminum atoms at T1/T2/T3/T4 positions of **FER** molecular sieves were 60.5, 51.5, 53.5, and 56.6 ppm, respectively.

In the synthesis process of zeolites, organic directing agents play a crucial role in balancing the negative charge introduced by the aluminum atoms in the framework. Consequently, these organic structural directing agents significantly influence the distribution of aluminum in molecular sieves. Pinar et al.[11,21,22] synthesized **FER** zeolites using a fluorinated system without the use of inorganic cations, using a combination of 1-benzoyl-1-methylpyrrolidinium (BMP), 2-hydroxymethyl-1-benzoyl-1-methylpyrrolidinium (bmprol) hydroxide, trimethylamine, pyridine, pyrrolidine, and several organic template agents. They investigated the synthesis of different organic structural directing agents. The distribution pattern of aluminum in the molecular sieve framework and its effect on the catalytic isomerization reaction of n-butene framework. Due to the different sizes of template molecules and their interactions with skeleton atoms, **FER** zeolites with different skeleton aluminum distributions can be obtained. When larger template molecule are used, a longer crystallisation time is required to increase the distribution probability of aluminium atoms in the 10-MR, enhance the BAS of the 10-MR, and improve the control of the activity and selectivity of n-butene skeleton isomerization reaction. Conversely, it tends to lead to side reactions such as olefin polymerization and cracking, and accelerate catalyst deactivation. In addition, the studies of Leshkov [23] and Chu [24] also indicate that when different sizes of cyclic or chain amines are used as organic structure directing agents, **FER** zeolites with different 10-MR and 8-MR aluminum distributions can also be obtained. Numerous studies have shown that the distribution of aluminum in the framework of zeolites is not only influenced by organic structural directing agents, but also by the synthesis conditions of zeolites [25], the silicon and aluminum sources used [26,27], solvents [28], inorganic cations [29–31], and post-treatment [32–34]. During the seed induced synthesis of molecular sieves, seed can play a role in reducing or avoiding the use of organic structure directing agents, shortening crystallization time, avoiding impurities, and regulating the crystal morphology of target zeolites [35–37]. Xiao et al. [38] believe that seed can be considered as the third type of structure directing agent. Zhang et al. [39] synthesized **FER** zeolite with good crystallinity, large surface area, uniform micropores, and abundant acidic sites using RUB-37 as the crystal seed. Studies by Ham et al. [40–42] showed a change in the distribution of framework aluminium atoms in seed-induced synthesized **FER** zeolites as compared to seed **FER** zeolites. The higher BAS content of the 8-MR than the 10-MR resulted in better dimethyl ether carbonylation activity and stability of the seed induced synthesised **FER** zeolites than seed. In addition, Nishitoba [26] found that when using trimethylamine as an organic structure directing agent to synthesize **CHA** molecular sieves, the addition of **FAU** molecular sieves as crystal seeds and aluminum sources can regulate the distribution of aluminum atoms in the framework of **CHA** molecular sieves. These studies indicate that the distribution of aluminium in the molecular sieve framework can be modulated using the seed induction methods.

In this work, the synthesis of **FER** zeolites under different conditions were investigated as fellow: organic structure directing agent synthesis, seed induced synthesis, and seed combining organic structure directing agent investigation. The distribution of aluminum atoms in the framework of **FER** zeolites synthesized by different methods and their catalytic performance for n-butene skeleton isomerization reaction were investigated. The obtained catalyst of FER-PY+SH exhibited unique distribution of skeletal aluminum， which enhanced the acidic strength in the 10-MR and significantly improved the catalytic activity and selectivity of **FER** zeolites for n-butene skeleton isomerization reaction. A new method for regulating the distribution of aluminum and acid in the framework of **FER** zeolites was proposed.

2. Results and Discussion

2.1. Structural and Textural Properties

As shown in Figure 1, XRD patterns of FER-PY, FER-SN, FER-SH, FER-PY+SN and FER-PY+SH exhibit typical diffraction peaks at 9.3°, 22.3°, 23.5°, 24.3°, 25.2°, 25.7° and 28.5° out of the (200), (321), (330), (112), (040), (202) and (312) crystal planes in **FER** topology (PDF #44-0104), respectively, indicating the successful formation of the **FER** zeolite without detectable impurities [19,20]. The relative crystallinity (R.C.s) was calculated by integrating the areas of diffraction peaks within 9.3-28.5°, and the sum of the areas of FER-PY was set as 100% for reference. As listed in Table 1, the calculated R.C.s values are comparable, measuring 101%, 99%, 100% and 101% for FER-SN, FER-SH, FER-PY+SN and SHFER-PY+SH, respectively. These results further demonstrate the excellent structure directing abilities of PY, SN, SH, PY+SN and PY+SH. The composition information is listed in Table 1, where the SiO_2 to Al_2O_3 ratios (SARs) of the five samples are within 24.6 - 25.6. Additionally, the Na_2O contents are all below 45 mg/g, suggesting that all FER-X samples have similar compositions and acidic densities. The calculated texture parameters are shown in Table 1, in line with the XRD observations, the specific surfaces and pore volumes remain relatively uniform, for instance, the values of S_{BET} average around 430 m^2/g, while V_{total} and V_{micro} are all about 0.27 cm^3/g and 0.14 cm^3/g, respectively.

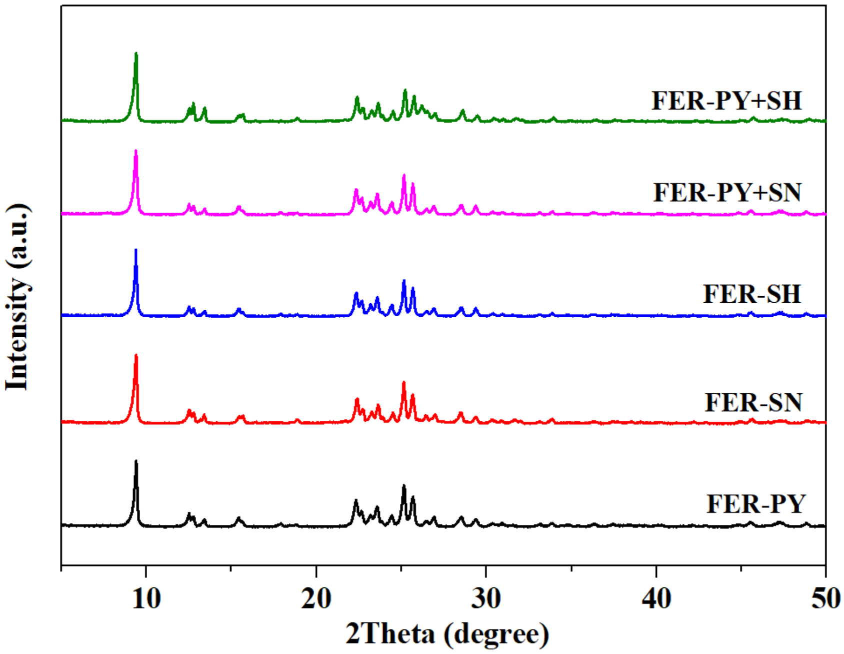

Figure 1. XRD patterns of of various FER-X zeolites.

Table 1. Textural properties of of various FER-X zeolites.

Sample	Na_2O (mg/g)	SARs	Crystallinity (%)	Surface Area (m^2/g)		Pore Volume (cm^3/g)	
				Total	Micro	Total	Micro

Preprints.org (www.preprints.org) | NOT PEER-REVIEWED | Posted: 3 September 2024 doi:10.20944/preprints202409.0175.v1

FER-PY	**40**	**25.6**	100	431	388	0.27	0.14
FER-SN	39	25.3	101	428	386	0.27	0.14
FER-SH	36	24.6	99	422	380	0.26	0.13
FER-PY+SN	42	25.3	100	430	378	0.28	0.14
FER-PY+SH	41	24.8	101	432	390	0.28	0.15

The SEM images (Figure 2) present the morphologies of the obtained FER-X zeolites. All samples are composed of hexagonal flake-like crystals with smooth surfaces; the average size of each flake is ~ 1 μm in length; ~ 500 nm in width and 20 ~ 50 nm in thickness. Combined XRD and TEM analyses indicate that their morphology and structure are identical.

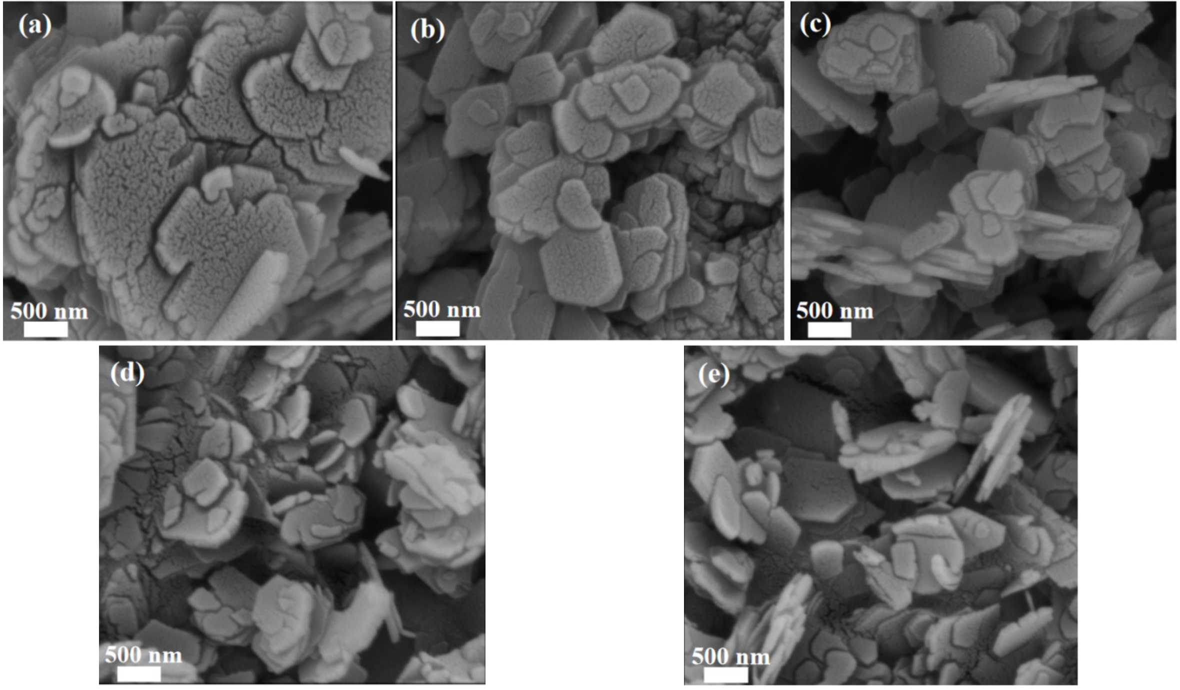

Figure 2. SEM images of various FER-X zeolites.

2.2. Acidity Characterization

The acidic properties were characterized using NH_3-TPD and Py-IR. As illustrated in Figure 3, two NH_3 desorption peaks are observed at 195 ^{o}C and 450 ^{o}C （Figure 3a）, corresponding tothe desorption of NH_3 molecules that interact with the weak acids and strong acids, respectively. The positions of of these peaks provide insight into acid strength, indicating the weak and strong acid sites in FER-X samples exhibit similar acidic densities. Figure 3 (b)-(f) shows the Py-IR spectrum extracted at 150 ^{o}C, 250 ^{o}C and 350 ^{o}C. The IR adsorption peak at 1450 cm^{-1} corresponds to the C-N stretching of pyridine adsorbed on LAS, while the peak at 1490 cm^{-1} is attributed to the C-H vibration of pyridine on both BAS and LAS. The peak at 1540 cm^{-1} is due to the N-H stretching of pyridinium cations generated by protonation of pyridine on BAS. As shown in the Figure 3 (b)-(f), with the increase of desorption temperature, both BAS and LAS in the sample decrease. When the desorption temperature reaches 350 ^{o}C, LAS decreases to a very low level, indicating a scarcity of strong LAS in the FER-X samples. In contrast,, the decrease in BAS is considerably smaller, indicating a stronger acidity of the BAS present in the FER-X samples.

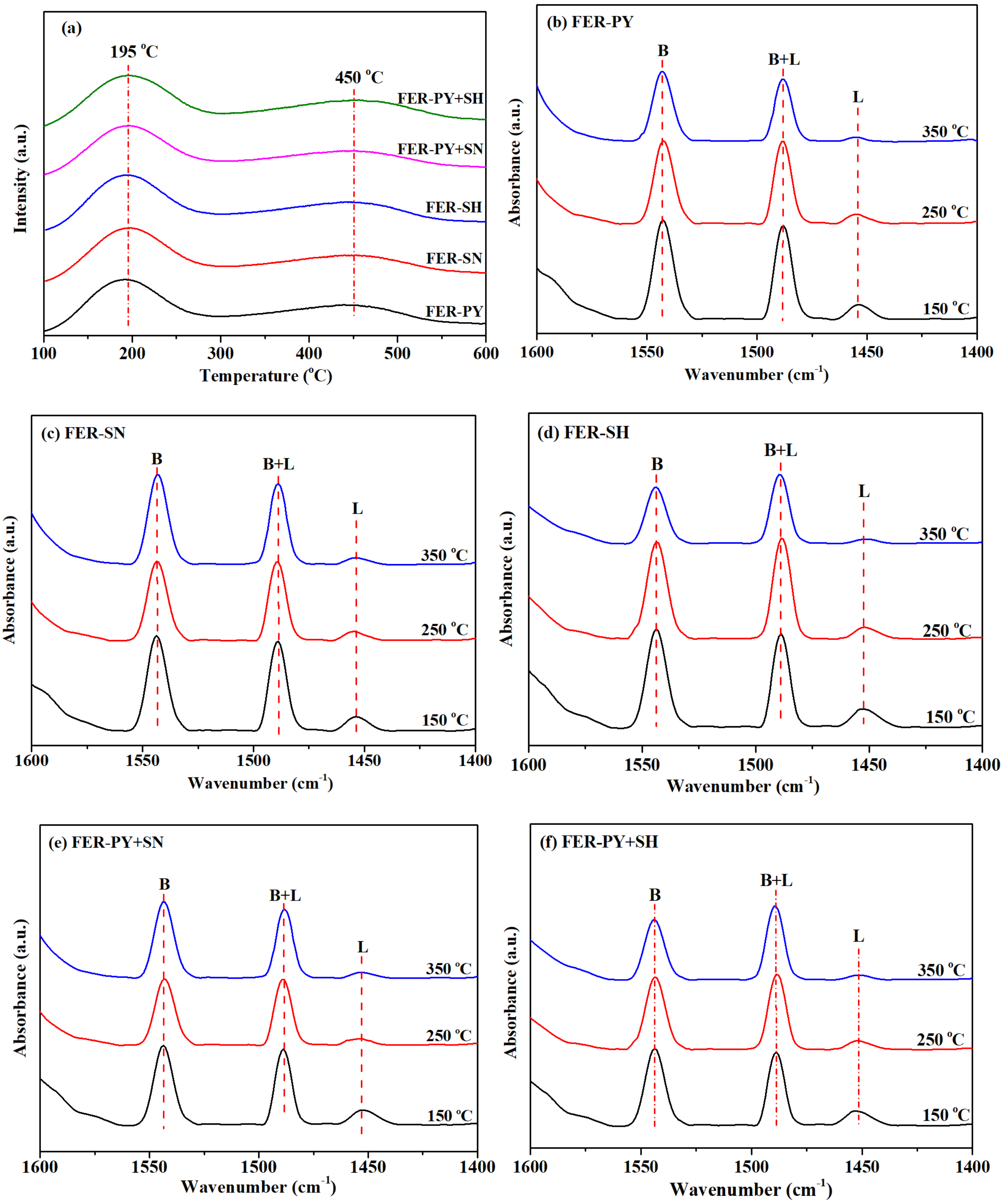

Figure 3. NH_3-TPD and Py--IR profiles of various FER-X zeolites.

The quantitative analysis of NH_3-TPD and Py-IR experiments is presented in Table 2. Notably, NH_3-TPD provides an overall assessment of the acidity of the samples, as the kinetic diameter of NH_3 (3.7 Å) is smaller than the 8-MR and 10-MR apertures in **FER** structure. In contrast, Py-IR could only detect the acid sites located in 10-MR due to its larger kinetic diameter (5.7 Å for pyridine vs. 4.8 Å for 8-MR). Consequently, the discrepancy between the total acid density acquired from NH_3-TPD and Py-IR can be used to elucidate the distribution of acid sites in the zeolites (see the caption below Table 2 for more details). From the NH_3-TPD, the overall acid distributions are similar， with acid densities approximately around 1.3 mmol/g for the five samples, consistent with their structural and compositional properties. However, more BAS can be identified over Py-IR for the FER-X samples (0.29 mmol/g for FER-PY and 0.28 ~ 0.34 mmol/g for others), especially for FER-PY+SH whose value is 0.34 mmol/g. In addition, the $B_{10\text{-}350}$ (350 denotes to the desorption temperature as measured from Py-IR) are also shown in Table 2, this value is 0.20 mmol/g for FER-PY and increases monotonically to 0.32 for FER-PY+SH. The differing acid distribution may arise from the distinct nucleation and crystal growth processes of zeolites synthesized using seed crystals, or a combination of seed crystals and organic templates, compared to those formed solely with organic templates. The different $B_{10\text{-}350}$ provides direct evidence that utilizing seeds or employing a combination of seeds and organic templates will alter the acid distribution in FER zeolite.

Table 2. Amounts of Acid in the Various FER-X Samples.

Sample	Acidity by NH_3-TPD[a] (mmol/g)			Acidity by Py-IR[b] (mmol/g)			
	Weak	**Strong**	**Total**	**Brønsted**	**Lewis**	**Total**	**$B_{10\text{-}350}$[c]**
FER-PY	0.79	0.56	1.35	0.29	0.03	0.32	0.20
FER-SN	0.78	0.55	1.33	0.28	0.03	0.31	0.24
FER-SH	0.75	0.53	1.28	0.28	0.03	0.31	0.25
FER-PY+SN	0.76	0.52	1.28	0.30	0.03	0.33	0.28
FER-PY+SH	0.81	0.56	1.37	0.34	0.02	0.35	0.32

a) Acid sites on HFER and their amounts were measured by NH_3-TPD analysis, and the amounts of weak and strong acid sites were calculated by using an integrated area at the maximum desorption temperatures of NH_3 at 195 °C and 450 °C, respectively.

b) Amounts of BAS and LAS were measured by pyridine FT-IR (Py-IR) spectroscopy at a desorption temperature of 150 °C and 350 °C, and the number of acid sites was calculated by using the well-known formula of B sites = $1.88A_BR^2/W$, L sites = $1.42A_LR^2/W$, where A_B and A_L are the integrated absorbance peak areas of BAS and LAS located at 1550 and 1450 cm^{-1}, respectively, and R represents the radius of a catalyst pellet of HFER with a catalyst weight W.

c) The number of BAS located in 10-MR at 350 °C was calculated by conducting PY-IR measurements at a desorption temperature of 350 °C.

2.3. 29Si and ^{27}Al MAS NMR

The ^{29}Si MAS NMR spectra show closely similar features (Figure 4), exhibiting four sub-peaks from the curve at approximately –100, –107, –112 and –116 ppm, respectively. The peaks at –100 and –107 ppm correspond to the Si atoms bonded to two Al atoms (Si(2Al)) and one Al atom (Si(1Al)), respectively. While the peak at –112 and –116 ppm can be attributed to the Si atoms that are not adjacent any Al atoms (Si(0Al)), silicon connecting to four Si tetrahedrons in the **FER** framework [18,43]. The weaker signal at –100 ppm of all samples indicates a lower prevalence of Al–O–Si–O–Al species on FER-X zeolites.

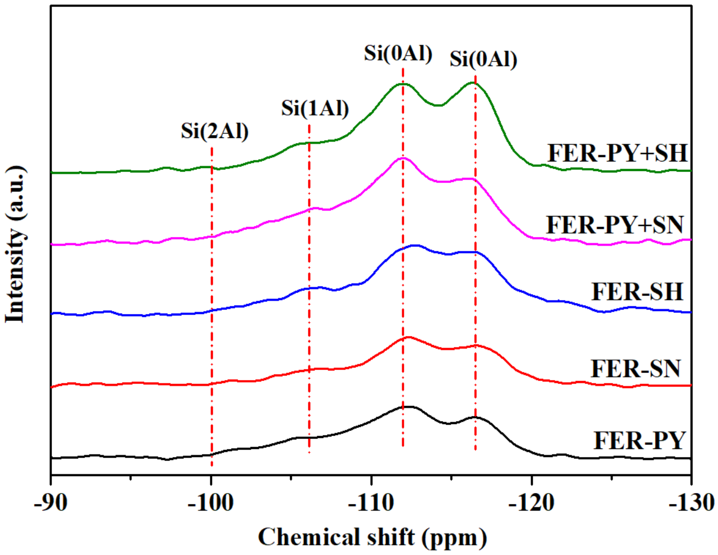

Preprints.org (www.preprints.org) | NOT PEER-REVIEWED | Posted: 3 September 2024

doi:10.20944/preprints202409.0175.v1

Figure 4. ^{29}Si MAS NMR spectra of various FER-X zeolites.

The ^{27}Al MAS NMR spectrum of various FER-X zeolites are shown in Figure 5. As shown in Figure 5 (a), all of the FER-X samples exhibit a prominent resonance peak at 55 ppm corresponding to tetrahedrally coordinated Al species, while no signal peak appears at 0ppm. This indicates that the aluminum atoms in zeolites samples are located on the skeleton of FER zeolites, and there are no framework aluminum present [39,40,44]. Previous studies have shown that aluminum atoms exhibit different NMR chemical shifts depending on their positions within the **FER** framework [18,20,43]. The ^{27}Al MAS NMR spectrum at 55 ppm is deconvolved into four peaks located at 61, 51, 53 and 58 ppm, respectively, as illustrated in Figure 5 (b)-(f). The Al population at T1-T4 sites in the FER-X samples was quantified from the corresponding ^{27}Al NMR spectra (Figure 5 (b)-(f)) and Table 3. The FER-PY sample exhibited a minimal fraction of Al atoms on the T1+T3 sites (30%). In comparison, the distribution proportion of aluminum on the T1+T3 positions in FER-SN, FER-SH, and FER-PY+SN gradually increased to 41%, 44%, and 50% respectively, while the distribution proportion of aluminum at T1+T3 positions on the FER-PY+SN reached the highest value of 60%. Notably, both samples contained a small amount of Al on the T1 site (0 ~ 12%).

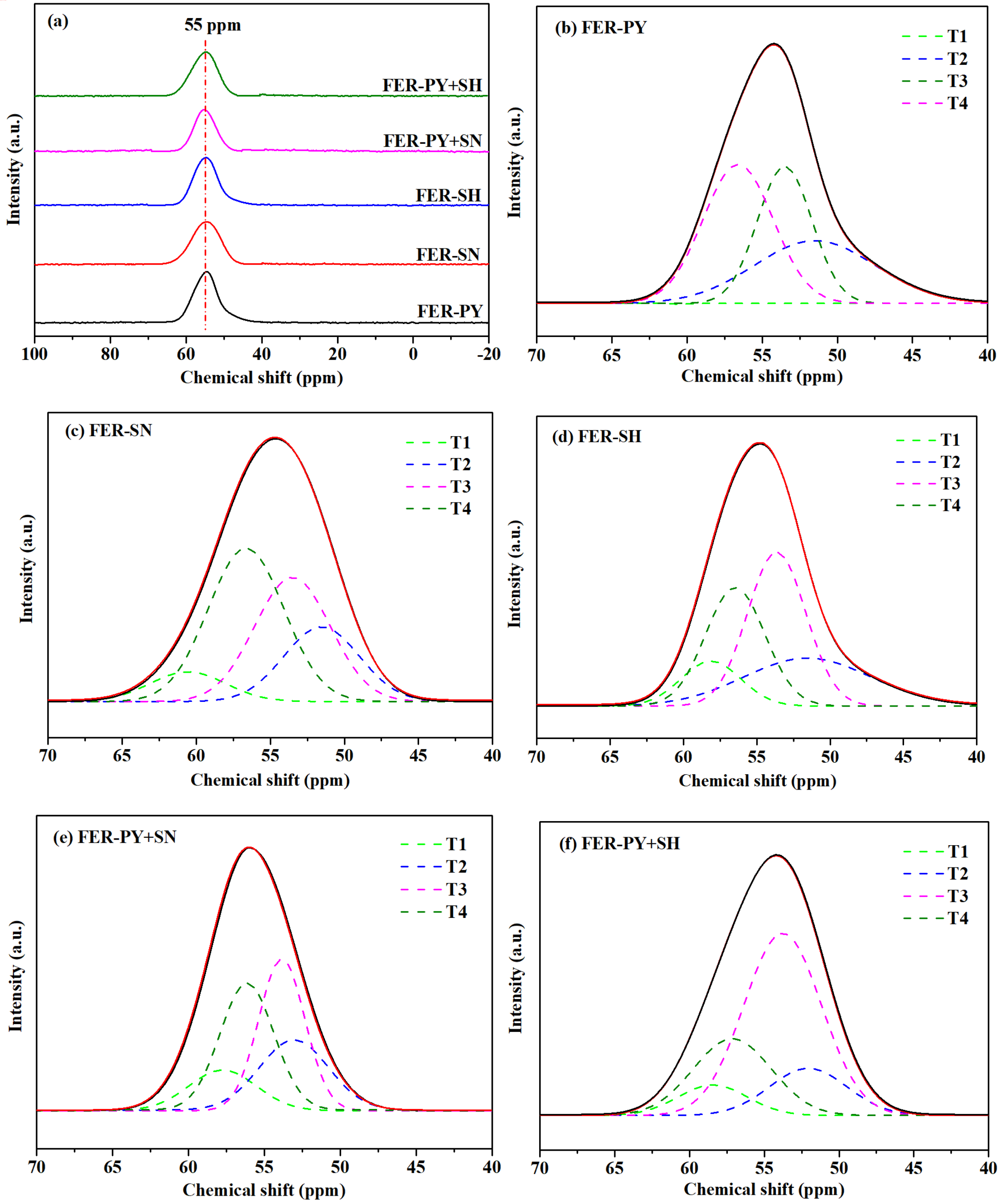

Preprints.org (www.preprints.org) | NOT PEER-REVIEWED | Posted: 3 September 2024 doi:10.20944/preprints202409.0175.v1

Figure 5. ^{27}Al MAS NMR spectra of various FER-x zeolites.

Table 3. Aluminum distribution obtained from the curve fifitting of ^{27}Al MAS NMR spectra of various FER-X zeolites.

Sample	**Aluminum Distribution (%)**				
	T1	**T2**	**T3**	**T4**	**T1+T3**
FER-PY	0	30	30	39	30
FER-SN	8	19	33	40	41
FER-SH	10	25	34	31	44
FER-PY+SN	12	21	38	29	50
FER-PY+SH	6	15	54	25	60

In summary,, compared to FER-PY synthesized with pyrrolidine, FER-X samples possess similar compositional and textural properties, with total acid densities are closely aligned. Nevertheless, the combined use of pyrrolidine and H-form FER seeds renders a distinctive acid distribution, with a greater number of strong acid sites located in the 10-MR. To elucidate the relationship between the Aluminum distribution and the acid distributions of FER-X zeolites, Figure 6 correlates the aluminum distribution data at T1+T3 positions of different samples with B_{10-350}. A linear relationship can be observed between T1+T3 and B_{10-350}, implying the acid distributions positively correlates with the quality of the aluminum distribution on the T1+T3. Several factors may contribute to this result. First, the use of seed crystals to facilitate FER zeolite synthesis accelerates the nucleation and crystallization processes, potentially leading to a higher distribution of aluminum within the 10-MR. Second, the lower sodium content in H-FER seeds allows for larger species to balance the framework charge, thereby increasing the likelihood of aluminum being positioned at T1+T3 sites in the 10-MR. Moreover, this effect is more pronounced in the presence of template agents alongside H-FER zeolite seeds.

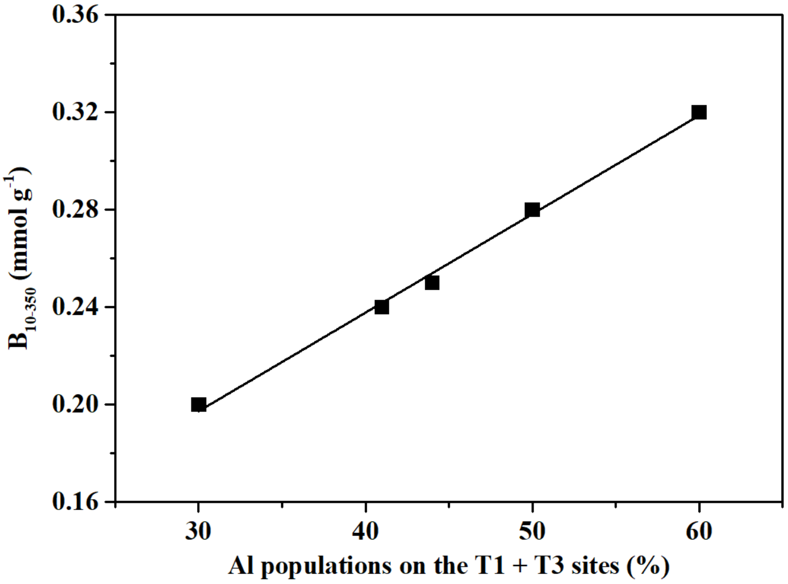

Figure 6. The influence of the Al distribution on the acid distribution of various FER-X zeolites.

2.4. Catalytic Performance

The catalytic performances of all FER-X samples in *n*-Butene isomerization are shown in Figure 7 using post-MTBE C4 as feed.

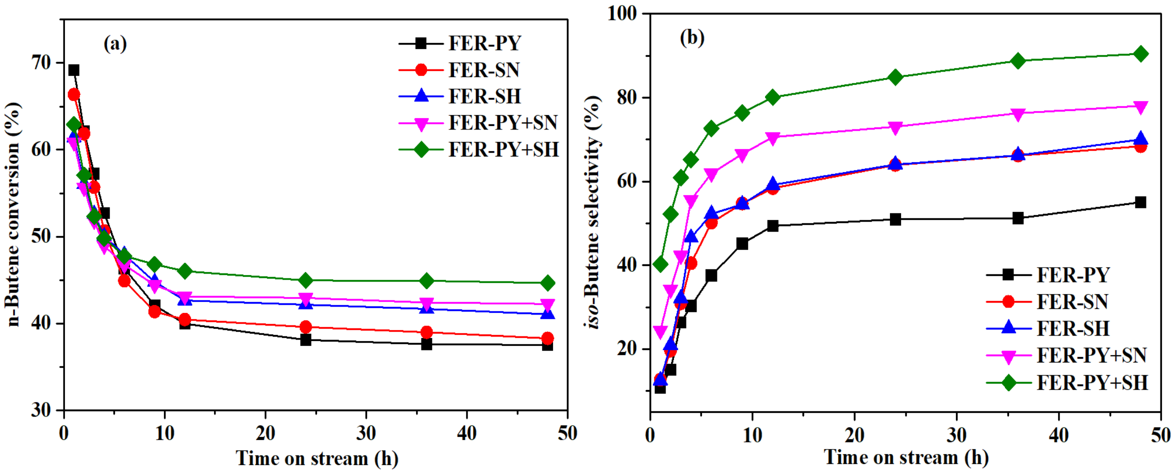

Figure 7. Catalytic performance of various FER-X zeolites for sketal isomerization of *n*-Butene from post-MTBE C4.

Figure. 7(a) illustrates the relationship between *n*-butene conversion against time on stream. Both FER-PY and FER-SN showed the best initial activities, achieving *n*-butene conversions exceeding 65%, while the initial conversions of the other samples fall within the range of 60% to 65%. As reaction proceeded, all conversions dropped rapidly during the first 12 h and then stabilized, approximately 45% after 48 h running.

In contrast to conversion trends, the selectivity of isobutene showed a completely reversed trend, the initial isobutene selectivity over FER-PY, FER-SN and FER-SH were below 20%, while FER-PY+SN and FER-PY+SH recorded selectivity of 25% and 40%, respectively. Then *isobutene* selectivity over FER-PY gradually increased to ~ 55% after 48 h. For FER-SN and FER-SH presented a sharp increase in the first 12 h and then kept steady, isobutene selectivity reached ~ 63% at 24 h. The isobutene selectivity over FER-PY+SN also presented a sharp increase in the first 12 h, leveling off at about 78% after 48 h. In contrast, FER-PY+SH achieved an even higher selectivity of 90%. The experimental results in Figure 7 are mainly due to the different acid distributions of the catalysts. The skeleton isomerization of *n*-butene to produce isobutene is carried out through the joint action of the monomolecular mechanism and the bimolecular mechanism[44–46]. In monomolecular mechanism, *n*-butene is first adsorbed and protonated into a carbenium cation on the acid site, after which it undergoes skeleton isomerization and proton-feedback to afford isobutene. Bimolecular mechanism mainly involves the polymerization and isomerization to generate various long-chain carbocations, which subsequently crack to produce isobutene and by-products such as propylene. In the initial stage of this reaction, the strong acid sites of **FER** zeolite were well-retained, resulting in the predominance of the bimolecular mechanism, which was followed by cracking and the generation of by-products. After the initial stage, carbon deposition began to cover the strong acid sites, leading to a decrease in catalyst activity while suppressing undesired side reactions. Previous investigations have proved that the BAS in 10-MR of **FER** zeolites are accountable for the skeleton isomerization of *n*-butene, while BAS in the 8-MR and LAS can exacerbate side reactions such as polymerization and cracking, despite their higher activity [47,48]. Therefore, FER-PY+SH demonstrates improved selectivity and isobuten yields owing to its higher $B_{10\text{-}350}$ concentration. As shown in Figure 8, the yield of isobutene increases with the increase of $B_{10\text{-}350}$ and Al distribution on the T1+T3.

Preprints.org (www.preprints.org) | NOT PEER-REVIEWED | Posted: 3 September 2024 doi:10.20944/preprints202409.0175.v1

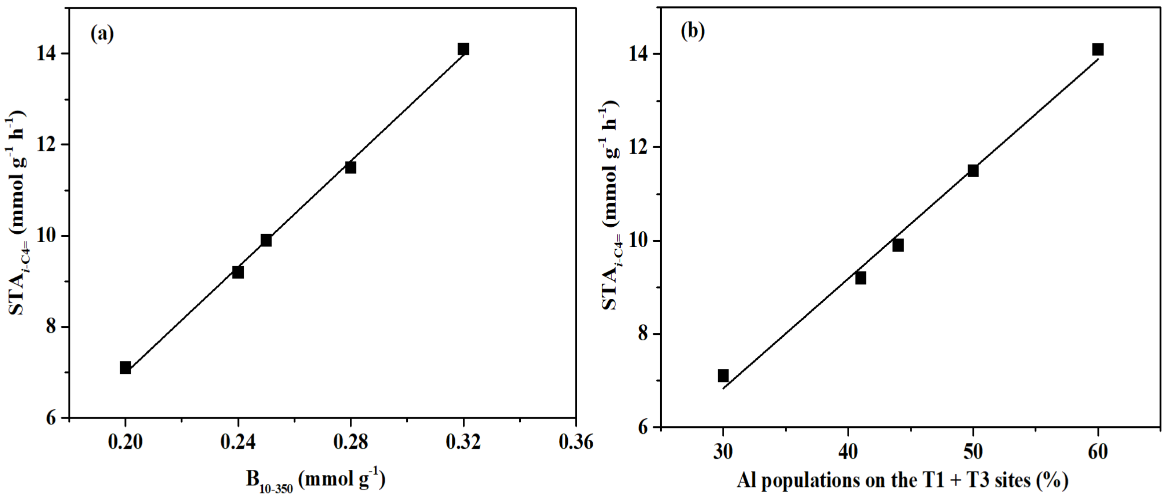

Figure 8. Relationship between STY$_{i\text{-C4=}}$ and strong BAS content in 10-MR channels (a) or Al distribution on the T1+T3 (b).

2.5. Catalyst Stability

Figure. 9 displays the long-term stability tests using FER-PY+SH as candidate catalysts. The catalytic results obtained with three recycles with regeneration (2160 h). The one-way life of the catalyst reaches 720 h, the conversion of n-butene is greater than 39%, the selectivity of isobutene is greater than 95%, and the yield of isobutene is greater than 37.5%. Interestingly, the activity and selectivity of FER-PY+SH in sketal isomerization of *n*-butene were fully recovered after each run. This finding substantiates that FER-PY+SH can be effectively reused, thereby extending its lifespan beyond most reported FER zeolites in the skeletal isomerization of n-butene. FER-PY+SH exhibits superior catalytic activity due to its unique distribution of skeletal aluminum and enhanced acidic strength in the 10-MR.

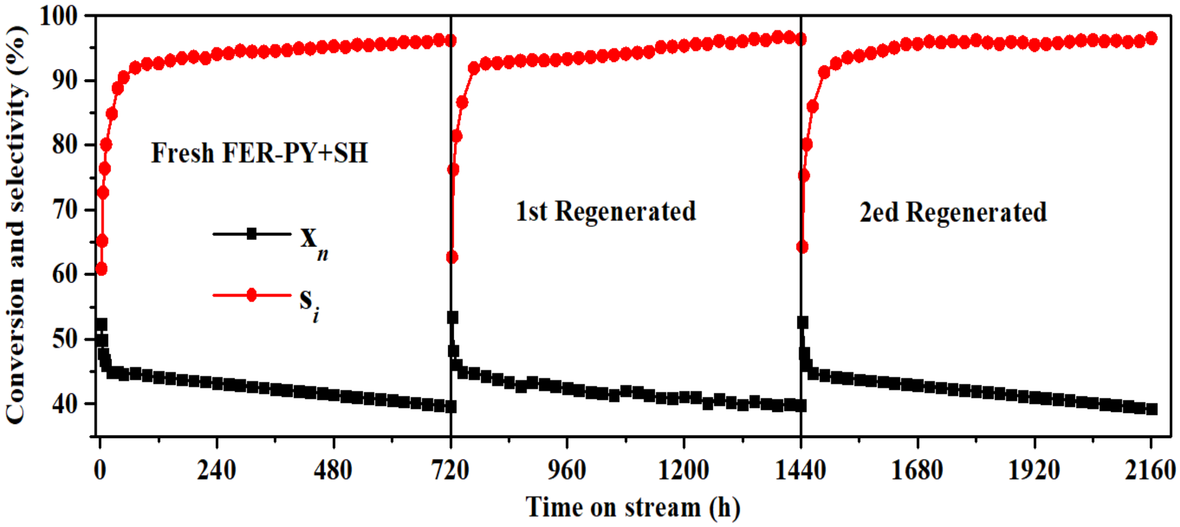

Figure 10. Stability of FER-PY+SH for sketal isomerization of *n*-butene. Reaction conditions: T=350 °C; p=0.1 MPa; WHSV$_{n\text{-Butene}}$=2.0 h^{-1}.

In conclusion, the preparation of FER-PY+SH zeolites using a combination of H-form seeds and pyrrolidine enriches the number of BAS in the 10-MR, effectively suppressing the bimolecular mechanism. The FER-PY+SH samples thus demonstrate excellent isomer selectivity and yields in the isomerization of n-butene.

Preprints.org (www.preprints.org) | NOT PEER-REVIEWED | Posted: 3 September 2024 doi:10.20944/preprints202409.0175.v1

3. Experimental

3.1. Materials

The reagents used for the synthesis of **FER** zeolite were silica sol (SS3015, 30% SiO_2, 0.02%NaO_2, Shandong Baite New Material Co., Ltd.), sodium metaaluminate ($NaAlO_2$, 99.0%, Tianjin Kermel Chemical Reagent Co., Ltd.), sodium hydroxide (NaOH, 96.0%, Tianjin Kermel Chemical Reagent Co., Ltd.), pyrrolidine (PY) (C_4H_9N, 99%, Tianjin Kermel Chemical Reagent Co., Ltd.), ammonium chloride (NH_4Cl, 99%, Tianjin Kermel Chemical Reagent Co., Ltd.), and deionized water.

3.2. Preparation of FER-X Zeolites

3.2.1. Preparation of Seeds

Typically, deionized water and NaOH aqueous solution were slowly added to silica sol (SiO_2, 30 wt%), and stirred vigorously for 1 h. Then, $NaAlO_2$ aqueous solution and pyrrolidine (PY) were added, followed by stirring for 2 h to form a homogeneous suspension with a molar composition of 0.1 Na_2O:0.033 Al_2O_3:1 SiO_2:25 H_2O:0.22 PY. The suspension was transferred into a Teflon-lined stainless-steel autoclave and crystallized at 160 °C under a rotation of 200 rpm for 72 h. After the hydrothermal synthesis, the product was washed with distilled water until it reached a neutral pH. Then dried at 120 °C overnight and calcinated at 550 °C in air for 6 h to obtain Na-form **FER**. The Na-form **FER** zeolites were subsequently converted into into NH_4-form via ion exchange with 1 mol/L NH_4Cl solution at 80 °C for 2 h, this process was repeated twice. Then, the resulting white slurry was filtered and dried at 120 °C for 6 h. Finally, H-form **FER** zeolite catalysts were obtained by calcination of NH_4-type **FER** zeolites in air at 500 °C for 4 h. These Na-form **FER** and H-form **FER** were used as the seeds.

3.2.2. Preparation of Seed-Derived FER-X zeolites

The seed-derived **FER** zeolites was prepared as fellows: organic structure directing agents were not used, while the remaining synthetic processes were kept identical to the procedures described above. Finally, the Na-form **FER** and H-form **FER** as seeds added to form homogeneous suspension with a molar composition of 0.1 Na_2O:0.033 Al_2O_3:1 SiO_2:25 H2O: 15% wt seeds. The prepared mother gel was transferred into a Teflon-lined stainless-steel autoclave and crystallized at 160 °C under a rotation of 200 rpm for 72 h, followed by centrifuging, rinsing, drying overnight at 120 °C to afford Na-form **FER**.

The method of synthesizing **FER** zeolites using both PY and Na-form **FER** or H-form **FER** as seeds simultaneously is similar to the synthesis methods of the two aforementioned **FER** zeolites. Finally, the homogeneous suspension with a molar composition of 0.1 Na_2O:0.033 Al_2O_3:1. SiO_2:25 H_2O: 0.12PY:15% wt seeds was transferred into a Teflon-lined stainless-steel reactor, and then hydrothermal synthesis was conducted for 72 h at 160 °C with 200 rpm. The white gel obtained after several washing steps and dried at 120 °C for 6 h, and further calcined at 550 °C in air for 6 h to afford Na-form **FER**.

3.2.3. Preparation of H-form FER zeolites

All of the Na-form **FER** zeolites were transformed into NH_4-form via ion exchange with 1 mol/L NH_4Cl solution at 80 °C for 2 h. This process that was repeated twice. Then, the resulting white slurry was filtered and dried at 120 °C for 6 h. Finally, H-form **FER** zeolite catalysts were obtained by calcining of NH_4-type **FER** zeolites in air at 500 °C for 4 h. The H-form **FER** zeolite prepared using PY was labeled as FER-PY, the H-form FER zeolite prepared by Na-form FER zeolites as seeds induction was denoted as FER-SN, the H-form FER zeolite prepared by H-form FER zeolites as seeds induction was denoted as FER-SH, and the H-form FER zeolite prepared PY and Na-form FER zeolites or H-form FER zeolites as seeds simultaneously was denoted as FER-PY+SN and FER-PY+SH respectively. Finally, the H-form **FER** zeolite was compressed and formed to obtain a catalyst for the skeletal isomerization of *n*-Butene.

3.3. Characterization of Catalysts

X-ray diffraction (XRD) was used to measure the crystallization and phase of the FER catalysts performed with a Rigaku D/max 2550 VB/PC diffractometer apparatus with Cu Ka radiation (λ = 0.15406 nm) at a voltage and current of 40 kV and 40 mA, respectively. The 2θ scanning range was from 5 to 40° with a scan rate of 4° / min and the step size of 0.02°. The R.C.s of the catalysts were obtained by calculating the sum of the peak intensity at 2θ = 9.3±0.1°, 22.3±0.1°, 23.5±0.1°, 24.3±0.1°, 25.2±0.1°, 25.7±0.1°, 28.5±0.1°, and the R.C.s of FER-PY was set as 100%.

The scanning electron microscopy (SEM) images of the samples were analyzed using a Nava Nano SEM 450 microscope to confirm the crystal morphology and size. The sodium content and SiO_2/Al_2O_3 molar ratio of the samples were determined by X-ray fluorescence (XRF) analysis by using a ZSX Primus II instrument operated at 60 kV and 150 mA. The textural characterization of the **FER** catalysts was performed by N_2 adsorption–desorption at -196 ℃ with a US Micromeritics ASAP 2020 V3.00 H nitrogen adsorption analyzer. The **FER** catalysts were outgassed at 350℃ for 5 h under the vacuum of 10^{-3} Pa to remove moisture and volatile impurities before the adsorption measurement. The specific surface areas were obtained by the Brunauer-Emmett-Teller (BET) method and the pore volume was calculated by N_2 adsorption at a relative pressure of 0.99.

The temperature-programmed desorption of ammonium (NH_3-TPD) with Micromeritics chemisorb 2720 instrument equipped with a thermal conductivity detector was used to study the acid properties of the catalysts. Typically, 150 mg of the sample was first preheated under a He stream of 30 mL·min^{-1} at 550℃ for 1 h, then purged in a 5% NH_3-He flow (30 mL·min^{-1}) at 100℃ for 40 min. Subsequently, the sample was treated under a He flow of 30 mL·min^{-1} at 100℃ for 60 min to remove the physically-adsorbed NH_3. Finally, the samples were heated from 100 to 550℃ using a temperature ramp of 10℃·min^{-1}, and the quantity of NH_3 desorbed was measured by a TCD detector.

Pyridine adsorption Fourier transform infrared (Py-IR) was used to determine B acid and L acid concentrations using a Bruker Tensor 27 infrared spectrometer. Approximately, the sample powder (30 mg) was formed into self-supporting wafer (dimeter 20mm) and then placed inside the reaction tank. The sample was degassed under vacuum at 500℃ for 2h under high vacuum conditions of 10^{-3} Pa, and then the sample was saturated with the probe molecule pyridine at 40℃ for 30 min, and subsequently, the physisorbed molecules were removed at 150 ℃ for 30 min. IR spectra was recorded at 350 ℃. The adsorption peaks located at 1540 cm^{-1} and 1450 cm^{-1} were assigned to B acid and L acid, respectively. The concentration of acid sites was calculated from the IR results using the extinction coefficient and integrated intensity of the desorption peak and the sample weight reported by Emeis [49].

Magic-angle-spinning nuclear-magnetic-resonance (MAS NMR) spectra of ^{27}Al and ^{29}Si were collected on a Bruker Avance III 600 MHz Wide Bore spectrometer (Bruker, Rheinstetten, Germany). The single-pulse sequence was adopted with a 10° pulse and a delay time of 0.3 s. The chemical shifts for ^{27}Al and ^{29}Si were calibrated by referring to $AlCl_3$ and tetramethylsilane, respectively. The ^{27}Al MAS NMR \ spectra were deconvoluted by using the mixed Gaussian–Lorentzian equation.

3.4. Catalyst Evaluation

The skeletal isomerization of n-butene was was conducted under atmospheric pressure in a fixed bed stainless-steel reactor unit, the tubular reactor having 12 mm inner diameter and 800mm length. Firstly, 3 g of the HFER catalyst (20-40 mesh) was placed in the middle of reactor, and the catalyst was pretreated under a N_2 flow at a heating rate of 10 ℃/ min, and the system was purged for 1 h. The feed stream of post-MTBE C4 was fed into the reactor by a mass flow controller to start the skeletal isomerization when heated to 350℃ at a weight hourly space velocity (WHSV) of n-butene was 2.0 h^{-1}. The properties of the post-MTBE C4 are listed in Table 4.

Table 4. Composition of post-MTBE C4 from refinery.

Composition	wt / %
Propane	0.12

Preprints.org (www.preprints.org) | NOT PEER-REVIEWED | Posted: 3 September 2024 doi:10.20944/preprints202409.0175.v1

Propylene	0.15
iso-Butane	52.86
Butane	10.94
trans-2-Butene	13.76
1-Butene	12.00
isobutene	0.26
cis-2-Butene	9.91

The products were analyzed using an Agilent 7890B gas chromatograph equipped with a flame ionization detector and an Agilent-GS-Alumina capillary column (50 m × 0.532 mm). Since the equilibrium of 1-butene, *trans*-2-butene, and *cis*-2-butene was established rapidly through double-bond isomerization at the temperature of the reaction, and all the straight-chain butene isomers were transformed to isobutylene, all of the straight-chain butene was considered as the *n*-butene reactant.

The conversion of *n*-butene (x_n) was defined as:

$$x_n = \frac{m_0 - m_1}{m_0} \times 100\% \quad (1)$$

The selectivity of isobutene (s_i) was defined as:

$$s_i = \frac{m_2 - m_3}{m_0 - m_1} \times 100\% \quad (2)$$

where m_0, m_1, m_2, and m_3 are the weights of *n*-Butene in the feed, the weights of *n*-Butene in the reaction products, the weights of isobutylene in the reaction products, and the weights of isobutylene in the feed, respectively.

The production rate of isobutene (space time yield, $STY_{iso\text{-}c4=}$) was defifined as the average moles of isobutene produced at the reaction duration of 24–48 h [mmol g^{-1} h^{-1}].

4. Conclusions

FER type zeolites have been successfully prepared in pyrrolidine as organic template or without pyrrolidine systems utilizing Na-form or H-form as seed. The seed derived **FER** samples own similar topological and morphological properties compared to the pyrrolidine derived one, as well as close total acid densities. The choice of H-form seed and pyrrolidine induces more BAS in the 10-MR of **FER** structure. As the BAS in 8-MR and LAS is responsible for the bimolecular mechanism that tends to cause more carbon depositions and side-products in *n*-Butene skeleton isomerization, the FER-PY+SH samples exhibit better isobutene selectivity and higher stability than the counterparts synthesized by Na-form as normal seed. By optimizing the synthetic parameters, the FER-PY+SH could be continuously operated for 720 h at 350 °C, 0.1 MPa for three recycles, and the *n*-butene mass space velocity of 2.0 h^{-1}, during which the *n*-butene conversion keeps higher than 39%, the selectivity of isobtene is higher 95%, and the *iso*-butene yield is higher than 37.5%.

Author Contributions: F.J.: investigation, data curation, writing—original draft. Z.X.: methodology, conceptualization, supervision, writing—review and editing. Y.F.: methodology, writing—original draft. X.Y.: methodology formal analysis, project administration. C.L.: validation, formal analysis. All authors have read and agreed to the published version of the manuscript.

Acknowledgments: The authors gratefully acknowledge the funding of the project by CNPC (2018B-1907).

Data Availability Statement: Not applicable.

Conflicts of Interest: The authors declare no conflict of interest.

References

1. Heriberto Díaz Velázquez, Likhanova N , Aljammal N ,et al. New Insights into the Progress on the Isobutane/Butene Alkylation Reaction and Related Processes for High-Quality Fuel Production. A Critical Review[J].Energy & Fuels, 2020, 34, 15525-15556.

Preprints.org (www.preprints.org) | NOT PEER-REVIEWED | Posted: 3 September 2024 doi:10.20944/preprints202409.0175.v1

2. Xu Q, Yang W, Chen Z, et al. Formation and regeneration of shape-selective ZSM-35 catalysts for n-Butene skeletal isomerization to isobutylene[J]. ACS Omega, 2018, 3, 8202-8211.
3. Corma A. Inorganic solid acids and their use in acid-catalyzed hydrocarbon reactions[J]. Chemical Reviews, 1995, 95, 559-614.
4. Houzvicka J, Ponec V. Skeletal isomerization of n -Butenes[J]. Catalysis Reviews. Science and Engineering, 1997, 39, 319-344.
5. Paul M, Naccache C. Skeletal isomerisation of n-butenes catalyzed by medium-pore zeolites and aluminophosphates[J]. Advances in Catalysis, 2010, 31, 505-543.
6. Vaughan P A. The crystal structure of the zeolite ferrierite[J]. Acta Crystallographica, 1966, 21, 983-990.
7. Xu H, Zhu J, Zhu L, Zhou E, Shen C. Advances in the synthesis of ferrierite zeolite[J]. Molecules, 2020, 25, 3722-3739.
8. Mooiweer H H, de Jong K P, Kraushaar-Czarnetzki B, Stork W H J, Krutzen B C H. Skeletal isomerisation of olefins with the zeolite ferrierite as catalyst[J]. Studies in Surface Science and Catalysis, 1994, 84, 2327-2334.
9. Wichterlová B, Ilkova N, Uvarova E, et al. Effect of Broensted and Lewis sites in ferrierites on skeletal isomerization of n-Butenes[J]. Applied Catalysis A General, 1999, 182, 297-308.
10. Domokos L, Lefferts L, Seshan K, et al. The importance of acid site locations for n-Butene skeletal isomerization on ferrierite[J]. Journal of Molecular Catalysis A Chemical, 2000, 162, 147-157.
11. Pinar A B, Márquez-álvarez C, Grande-Casas M, et al. Template-controlled acidity and catalytic activity of ferrierite crystals[J]. Journal of Catalysis, 2009, 263, 258-265.
12. Seo G, Jeong H S, Hong S B, et al. Skeletal isomerization of 1-Butene over ferrierite and ZSM-5 zeolites: Influence of zeolite acidity[J]. Catalysis Letters, 1996, 36, 249-253.
13. Donk S V, Bus E, Broersma A, et al. Probing the accessible sites for n-Butene skeletal isomerization over aged and selective H-Ferrierite with d3-acetonitrile[J]. Journal of Catalysis, 2002, 212, 86-93.
14. Corma, A. From Microporous to Mesoporous Molecular Sieve Materials and Their Use in Catalysis[J]. Chem. ReV. 1997, 97, 2373-2420.
15. Li J, Gao M, Yan W, et al. Regulation of the Si/Al ratios and Al distributions of zeolites and their impact on properties[J]. Chem. Sci., 2023, 14, 1935-1959
16. Mercedes,B; Corma A. What Is Measured When Measuring Acidity in Zeolites with Probe Molecules?[J]. ACS Catalysis, 2019, 9, 1539-1548.
17. Palcic A V V. Analysis and control of acid sites in zeolites[J]. Applied Catalysis, A. General: An International Journal Devoted to Catalytic Science and Its Applications, 2020, 606, 117795.
18. Xiong Z P, Qi G D, Bai L Y, et al. Preferential population of Al atoms at the T4 site of ZSM-35 for the carbonylation of dimethylether[J]. Catal. Sci. Technol., 2022, 12, 4993-4997.
19. Bohinc R, Hoszowska J, Dousse J C, et al. Distribution of aluminum over different T-sites in ferrierite zeolites studied with aluminum valence to core X-ray emission spectroscopy[J]. Physical Chemistry Chemical Physics, 2017, 19, 29271-29277.
20. Pinar A B, Verel R, Pariente P P, et al. Direct evidence of the effect of synthesis conditions on aluminum sitting in zeolite ferrierite: A ^{27}Al MQ MAS NMR study[J].Microporous and Mesoporous Materials, 2014, 193, 1-17.
21. Pinar A B, Hortiguela L G, McCusker L B, et al. Controlling the Aluminum Distribution in the Zeolite Ferrierite via the Organic Structure Directing Agent[J]. Chem. Mater., 2013, 25, 3654-3661.
22. Alvarez C M, Pinar A B, García R, et al. Influence of Al distribution and defects concentration of ferrierite catalysts synthesised from na-free gels in the skeletal isomerisation of n-Butene[J]. Top Catal, 2009, 52, 1281-1291.
23. Leshkov Y R, Moliner M, Davis M E. Impact of Controlling the Site Distribution of Al Atoms on Catalytic Properties in Ferrierite-Type Zeolites[J]. J. Phys. Chem. C, 2011, 115, 1096-1102.
24. Chu W F, Liu X N, Yang Z Q, et al. Constrained Al sites in FER-type zeolites[J]. Chinese Journal of Catalysis, 2021,42, 2078-2087.
25. Kim S, Park G, Woo M H, et al. Control of hierarchical structure and framework-Al distribution of ZSM-5 via adjusting crystallization temperature and their effects on methanol conversion[J]. ACS Catalysis, 2019, 9, 2880-2892.
26. Gabova V, Dedecek J, Cejka. Control of Al distribution in ZSM-5 by conditions of zeolite synthesis[J]. J. Chem. Commun. 2003,10, 1196-1197.
27. Nishitoba T, Yoshida N, Kondo J N, et al.Control of Al distribution in the CHA-type aluminosilicate zeolites and its impact on the hydrothermal stability and catalytic properties[J]. Ind. Eng. Chem. Res, 2018, 57, 3914-3922.
28. Heard C J, Luká G, Nachtigall P. The effect of water on the validity of Lwenstein's rule[J].Chemical Science, 2019, 10, 5705-5711.
29. Iorio J R D, Gounder R. Controlling the isolation and pairing of aluminum in Chabazite zeolites using mixtures of organic and inorganic structure-directing agents[J]. Chem. Mater., 2016, 28, 2236-2247.

Preprints.org (www.preprints.org) | NOT PEER-REVIEWED | Posted: 3 September 2024 doi:10.20944/preprints202409.0175.v1

30. Iorio J R D, Li S , Jones C B, et al. Cooperative and competitive occlusion of organic and inorganic structure directing agents within Chabazite zeolites influences their aluminum arrangement[J]. Journal of the American Chemical Society, 2020, 142, 4807-4819.
31. Fletcher R E, Ling S, Slater B. Violations of Löwensteins rule in zeolites[J]. Chem Sci, 2017, 8, 7483-7491.
32. Inagaki S, Yamada N, Nishii M, et al. Control of framework Al distribution in ZSM-5 zeolite via post-synthetic $TiCl_4$ treatment[J]. Microporous and Mesoporous Materials, 2020, 302, 1102231-1102239.
33. Vjunov A, Fulton J L, Huthwelker T, et al. Quantitatively Probing the Al Distribution in Zeolites[J]. Am. Chem. Soc., 2014, 136, 8296-8306.
34. Holzinger J, Beato P, Lundegaard, L F, et al. Distribution of Aluminum over the tetrahedral sites in ZSM-5 zeolites and their evolution after steam treatment[J]. The journal of physical chemistry, C, Nanomaterials and interfaces, 2018, 122, 15595-15613.
35. Meng X J, Xiao F S. Green routes for synthesis of zeolites[J]. Chemical Reviews. 2014, 114, 1521-1543.
36. Ye Z, Zhang H, Zhang Y, et al. Seed-induced synthesis of functional MFI zeolite materials:Method development, crystallization mechanisms, and catalytic properties[J]. Front. Chem. Sci. Eng., 2020, 14, 1-16.
37. Zhang H, Zhao Y, Zhang H, et al. Tailoring zeolite ZSM-5 crystal morphology porosity through flexible utilization of Silicalite-1 seeds as templates: Unusual crystallization pathways in a heterogeneous system[J]. Chemistry-A European Journal, 2016, 22, 7141-7151.
38. Ji Y, Wang Y, Xie B, et al. Zeolite Seeds: Third Type of Structure Directing Agents in the Synthesis of Zeolites[J]. Comments on Inorganic Chemistry, 2016, 36, 1-16.
39. Zhang H, Guo Q, Ren L, et al. Organotemplate-free synthesis of high-silica ferrierite zeolite induced by CDO-structure zeolite building units[J]. Journal of Materials Chemistry, 2011, 21, 9494-9497.
40. Ham H, Junga H S, Kim H S, et al. Gas-phase carbonylation of dimethyl ether on the stable seed derived Ferrierite[J]. ACS Catal, 2020, 10, 5135-5146.
41. Kima J, Hama H, Junga H S, et al. Dimethyl ether carbonylation to methyl acetate over highly crystalline zeolite-seed derived Ferrierite[J]. Catalysis Science & Technology, 2018, 8, 3060-3072.
42. Kwak S J, Kim H S, Park N, et al. Recent progress on Al distribution over zeolite frameworks: Linking theories and experiments[J]. Korean J. Chem. Eng., 2021, 38, 1117-1128.
43. Guo Y X, Wang S, Geng R, et al. Enhancement of the dimethyl ether carbonylation activation via regulating acid sites distribution in FER zeolite framework[J]. iScience, 2023, 26: 1-13.
44. Xue T, Li S S, Wu H H.Surfactant-promoted synthesis of hierarchical zeolite ferrierite nano-sheets[J]. Microporous and Mesoporous Materials, 2021, 312, 1107481-1107488.
45. Xie S J, Peng J B, Xu L Y, et al. Synthesis of ZSM-35 zeolite using cyclohexylamine as organic template and its catalytic performance[J]. Chinese Journal of Catalysis, 2003, 24, 531-534.
46. Houzvicka J, Nienhuis J G, Ponec V. The role of the acid strength of the catalysts in the skeletal isomerisation of *n*-Butene[J]. Applied Catalysis A General, 1998, 174, 207-212.
47. Xu W Q , Yin Y G , Suib S L , et al. Modification of non-template synthesized ferrierite/ZSM-35 for n-Butene skeletal isomerization to isobutylene[J]. Journal of Catalysis, 1996, 163, 232-244.
48. Raúl A. Comelli. Skeletal Isomerization of Linear Butenes on Boron Promoted Ferrierite: Effect of the Catalyst Preparation Technique[J]. Catalysis Letters, 2008, 122, 302-309.
49. Emeis C A . Determination of Integrated Molar Extinction Coefficients for Infrared Absorption Bands of Pyridine Adsorbed on Solid Acid Catalysts[J]. Journal of Catalysis, 1993, 141, 347-354.

Disclaimer/Publisher's Note: The statements, opinions and data contained in all publications are solely those of the individual author(s) and contributor(s) and not of MDPI and/or the editor(s). MDPI and/or the editor(s) disclaim responsibility for any injury to people or property resulting from any ideas, methods, instructions or products referred to in the content.